International Journal of Adhesion & Adhesives 51 (2014) 67–80

Contents lists available at ScienceDirect

International Journal of Adhesion & Adhesives

journal homepage: www.elsevier.com/locate/ijadhadh

Analysis of cohesive failure in adhesively bonded joints with the SSPH meshless method

C.L. Tsai [a], Y.L. Guan [a], D.C. Ohanehi [a], J.G. Dillard [b], D.A. Dillard [a], R.C. Batra [a,*]

[a] Department of Engineering Science and Mechanics, M/C 0219, Virginia Polytechnic Institute and State University, Blacksburg, VA 24061, USA
[b] Department of Chemistry, M/C 0212, Virginia Polytechnic Institute and State University, Blacksburg, VA 24061, USA

ARTICLE INFO

Article history:
Accepted 12 February 2014
Available online 20 February 2014

Keywords:
Fracture simulations
Double cantilever beam
Cohesive zone model (CZM)
CZM parameters
Symmetric smoothed particle hydrodynamics basis functions

ABSTRACT

Adhesives have become the method of choice for many structural joining applications. Therefore, there is a need for improved understanding of adhesive joint performance, especially their failure, under a variety of loading conditions. Various numerical methods have been proposed to predict the failure of adhesive bonded material systems. These methods generally use a cohesive zone model (CZM) to analyze crack initiation and failure loci. The CZM incorporates a traction–separation law which relates the jump in surface tractions with the jump in displacements of abutting nodes of the cohesive segment; the area under the curve relating these jumps equals the energy release rate which is determined from experimental data. Values of parameters in the CZM are usually obtained through the comparison of results of numerical simulations with the experimental data for pure mode I and mode II deformations. Here a numerical approach to simulate crack initiation and propagation has been developed by implementing CZM in the meshless method using the symmetric smoothed particle hydrodynamics (SSPH) basis functions, and using the design of experiments technique to find optimal values of CZM parameters for mode I failure. Unlike in the finite element method where a crack generally follows a path between element boundaries, in the meshless method a crack can follow the path dictated by the physics of the problem. The numerical technique has been used to study the initiation and propagation of a crack in a double cantilever beam under mode I and mixed mode in-plane loadings. Computed results are found to agree well with the corresponding experimental findings. Significant contributions of the work include the determination of optimum values of CZM parameters, and simulating mode I, mode II and mixed mode failures using a meshless method with the SSPH basis functions.

1. Introduction

Fracture behavior in adhesively bonded material systems subjected to single mode or mixed mode loading is of significant interest in a number of industries, including those engaged in biomedical implants, construction, microelectronics, mining, transportation, and energy. In linear elastic fracture mechanics (LEFM), the critical value of either the stress intensity factor (SIF), or the maximum principal stress at a fixed distance from the crack tip, or the strain energy release rate (SERR) is used to simulate crack initiation. Alternatively, one can use the cohesive zone model (CZM) [1–3] to simulate crack initiation and propagation. The CZM has been developed to represent at the continuum level what happens at the atomic level during failure which can be thought of as breaking of bonds between adjacent atoms. Barenblatt [1] proposed a CZM that accounts for the interaction between several neighboring atoms which at the continuum level may be thought of as material points. Dugdale [2] considered a similar CZM to simulate yielding near a crack tip in an elastic–plastic material. The CZM is often used to analyze fracture problems in monolithic and composite materials because it avoids precisely capturing stress singularities near a crack tip. The CZM describes material separation with a traction–separation relation. Different forms of the relation have been developed [4] but they all have similar characteristics. As the cohesive surfaces start to separate, either the normal or the tangential or both tractions increase until a maximum value is reached, and subsequently the tractions decrease with an increase in the separation and become zero at complete separation. The fracture energy of the material is characterized by area under the traction–separation curve. Computed results usually depend upon the initial slope of this curve, the peak value of the traction and on the value of cohesive energy, which is not in general equal to the fracture toughness. Elices et al. [5] used inverse analysis procedure and the experimental data to determine the softening function in

* Corresponding author. Tel.: +1 540 2316051.
E-mail address: rbatra@vt.edu (R.C. Batra).

http://dx.doi.org/10.1016/j.ijadhadh.2014.02.009
0143-7496

the CZM for different materials such as concrete, polymethylmethacrylate and steel. Experimentally observed crack paths and failure loads were well predicted by introducing the determined softening function.

The CZM has been used in conjunction with the finite element method (FEM) to simulate fracture in metals, debonding in adhesives and delamination in composite materials [5–10]. Xu and Needleman [3] have analyzed dynamic crack propagation in a centered crack plate under tensile loading using the CZM. Hattiangadi and Siegmund [6] have applied the CZM approach to analyze coupled thermo-mechanical deformations of composite laminates with delamination cracks under a temperature gradient loading. Klein et al. [7] used the CZM approach including a finite material strength and the work of fracture to study failure of brittle materials. Meshfree methods were used to adaptively insert cohesive surfaces at locations where the potential crack based on fracture mechanics considerations may initiate. Love and Batra [11] have adopted a similar approach of adaptively introducing cohesive surfaces at inter-element boundaries where fractures may initiate based on the analysis of transient deformations of a thermo-elasto-visco-plastic particulate composite.

Two different traction–separation relations, namely exponential and piecewise linear, were used by Li and Chandra [8] to study crack initiation and crack growth resistance in elastic–plastic materials. They concluded that the crack growth resistance depends on the cohesive strength, the cohesive energy and the shape of the traction–separation curve. Sorensen and Jacobsen [9] used the J-integral based approach to determine the cohesive relation for a unidirectional glass fiber-epoxy double cantilever beam (DCB) laminate with uneven bending moments applied to two segments of the DCB. They found that the mixed mode cohesive stresses depend on the normal and the tangential crack opening displacements. Zhang and Paulino [10] used the CZM to study the fracture of functionally graded materials. They delineated the effect of different material gradations on crack initiation and propagation under mode I and mixed mode loading, compared numerical results with the corresponding experimental observations, and concluded that the CZM can be used to satisfactorily analyze the fracture behavior of FGMs.

The meshless method using the moving least squares (MLS) basis functions and the CZM has been used in [12] to simulate mode I failure and delamination under quasistatic loading. Barbieri and Meo [13] used the CZM and the reproducing kernel particle method (RKPM) basis functions to study crack initiation and propagation in composites. When using the MLS and the RKPM basis functions to approximate a function f, the computation of derivatives of f requires that the kernel function used to generate basis functions be differentiable. However, this is not the case in the SSPH basis functions. Zhang and Batra [14] have elaborated upon differences between the SSPH, RKPM, MLS and FE basis functions. In [15] we discussed the relative performance of the MLS and the SSPH basis functions when analyzing crack initiation and propagation problems in monolithic materials. Here we use the CZM and the SSPH basis functions to study crack initiation and propagation of adhesively bonded joints. Qian et al. [31] have compared meshless methods with the FEM. A major advantage of a meshless method over the FEM for crack propagation problems is that a crack path is independent of the distribution of particles in the domain whereas in the FEM it depends upon the mesh design.

The rest of the paper is organized as follows. In Section 2 we briefly summarize the approach and defer to the Appendix the review of the SSPH basis functions, and a weak formulation of the problem including cohesive segments used to simulate failure initiation and propagation. Experimental work is briefly reviewed in Section 3. In Section 4 the method of manufactured solutions is

Table 1
Comparison of the SSPH/MLPG method and the FEM for crack propagation in elasto-dynamic problems.

	SSPH/MLPG	FEM
Weak form	Local	Global
Data preparation effort	Little	Considerable
Basis functions	Not necessarily polynomials	Polynomials
Support of basis functions	Compact	Compact
Continuity of basis functions	Continuously differentiable	Normal derivatives discontinuous across element boundaries
Stresses and strains	Good everywhere	Good values at integration points
Integration rule	Higher order (cannot be easily determined)	Lower order (can be estimated)
Addition of nodes/particles	Easy	Involves considerable work
Information needed about nodes	Locations	Locations and element connectivity
Subdomains/elements	Circular/rectangular, not necessarily disjoint	Polygonal and disjoint
Crack paths	Dictated by physics of the problem	Generally along element boundaries
Stress singularities	Need enriched basis functions	Need enriched basis functions
Derivatives of basis functions	Different basis functions for the trial solution and its derivatives	Basis functions for derivatives derived by differentiating basis functions for the trial solution
Satisfaction of essential boundary conditions	Requires extra effort	Easy to enforce
Mass and stiffness matrices	Asymmetric, large band width, not necessarily positive definite	Symmetric, banded, mass matrix positive definite, stiffness matrix positive definite after enforcing essential boundary conditions
Sum of elements of mass matrix	Not necessarily equal to the total mass of the body	Equal to total mass of the body
Mass lumping	Generally not used	Generally used
Assembly of equations	Not required	Needed
Time step size for explicit algorithms	Generally difficult (not possible unless the mass matrix is diagonalized)	Relatively easy
Total strain energy of the body	Difficult (because of overlapping domains used in the weak formulation)	Easy
Deletion of failed regions	Delineation of failed regions requires serious effort	Relatively easy because of the assumption of element failure
Continuity conditions at interfaces between two materials	Requires using either the method of Lagrange multipliers, jump function, or discontinuous basis functions	Relatively easy
Locking phenomenon for constrained problems	No	Yes
Implementation of CZM	Requires some effort	Easy

used to verify the in-house developed code. Numerical results obtained using this software for failure of pre-cracked DCB specimens are compared with the corresponding experimental findings in Section 4 to show dependence of the computed results upon values of CZM parameters. In Section 5, we describe a technique to find optimum values of CZM parameters. We use these values of variables to analyze the failure of DCB specimens under a variety of loading conditions in Section 6 and compare predictions from the mathematical/computational model with the corresponding experimental results. Conclusions of this work are summarized in Section 7.

2. Approach

We numerically and experimentally study crack propagation in an adhesively bonded joint, find optimum values of parameters in the CZM relation, and compare computed results with the experimental ones for different loading conditions. As suggested by a referee, we refer the reader to the Appendix for the pertinent equations, and have summarized in Table 1 differences between the SSPH basis functions with the meshless local Petrov–Galerkin formulation used here and the traditional FEM.

3. Experimental work

DCB specimens were prepared and tested to study the failure behavior of adhesively bonded systems, and find mode I and mode II fracture energies of the adhesive layer to be used in the numerical work. By comparing the test findings with predictions from simulations, we will validate the mathematical model of the problem.

3.1. Standard DCB specimen

DCB specimen adherends consisted of rectangular aluminum 6061-T6511 bars with nominal dimensions of $305\times25.4\times12.7\ \text{mm}^3$, and having 6 mm diameter holes for loading pins drilled 10 mm from one end of each adherend. The adherends were abraded with #220 sandpapers, rinsed with de-ionized (DI) water for 2 min, and then heated in an oven at 110 °C for 1 h to remove moisture from their surfaces.

The adherends were chemically treated by placing them in 10% (weight) NaOH solution for 10 min, rinsing with DI water for 2 min, placing them in HNO_3:H_2O=1:1 (volume) until gray surfaces appeared white metallic to the naked eye. The adherends were rinsed again with DI water for 2 minutes, and then placed in an oven heated to 110 °C for an hour. A commercial epoxy adhesive (J-B INDUSTRO-WELD structural adhesive, J-B Weld Company, Sulfur Springs, TX 75483, USA) was used to bond the adherends. The epoxy and hardener were mixed according to manufacturer's specifications. For bonding after drying, two shims were placed at the two ends to control bondline thickness at 0.3 mm. After applying the adhesive, the two adherends were held with C-clamps to maintain alignment. Each specimen was cured at room temperature for 24 h, minimizing residual thermal stresses caused from thermal effects of chemical reactions. The initial crack length was created in the adhesive by conducting the pure mode I test (e.g., see Fig. 1 below) and loads were released once the crack length reached the setup value.

3.2. Fracture energy of DCB specimen

Testing of the specimens was conducted on a dual actuator load frame described in Refs. [19,20]. The bonded end of the adherends was clamped in a vise at the base, and actuators could independently apply loads through clevises and loading pins attached to the two arms at the debonded end of the specimen, allowing for control of mode mixity. The fracture energy was calculated with the corrected beam theory (CBT) [21,22] that includes corrections to the measured crack length due to the transverse shear stress and the beam root rotation at the crack tip and the clamping point. Under the hypothesis of infinitesimal elastic deformations, stress fields resulting from mixed mode loadings can be obtained by linear superposition of the stress fields resulting from pure mode I and pure mode II loadings. Therefore, loads applied on the adherends in Fig. 1 can be partitioned into loads for mode I and mode II components as follows:

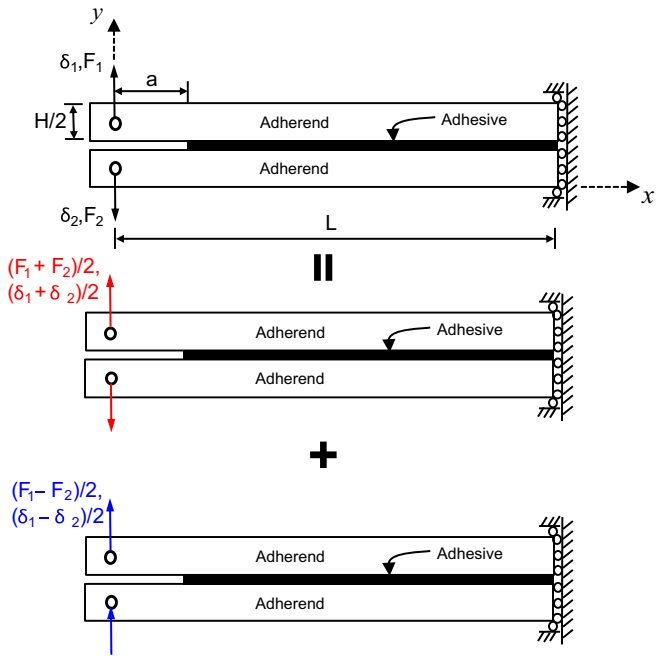

Fig. 1. Splitting of loads into pure mode I and mode II deformations of the DCB specimen.

$$F_I = (F_1+F_2)/2,$$
$$F_{II} = (F_1-F_2)/2, \tag{3.1}$$

where subscripts I and II denote mode I and II components, respectively. Positive values of F_1 and F_2 imply, respectively, forces acting on the top and the bottom adherends as shown in Fig. 1, and δ_1 and δ_2 represent the applied displacement on the top and bottom adherends, respectively. The mode I component of the applied strain energy release rate (SERR, or G_I) is calculated by using the equation [21]:

$$G_I = \frac{F_I^2(a+\Delta)^2}{BEI},$$
$$I = \frac{1}{12}Bh^3, \tag{3.2}$$

where a is the observed crack length, B is the width of the adherend, E and h are, respectively, Young's modulus of the adherend material and the thickness of one adherend, Δ is the correction to the crack length calculated from the negative intercept of the plot of $C^{1/3}$ versus the crack length in the mode I test as shown in Fig. 2; here C (compliance)$=\delta/F_I$. The crosshead displacement rate is set at 0.1 mm/min for a quasi-static analysis.

The mode II component of the SERR is given by [22]:

$$G_{II} = \frac{9F_{II}^2(a+0.42\Delta)^2}{EB^2h^3}, \tag{3.3}$$

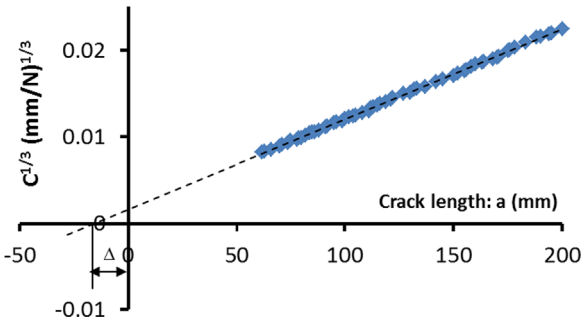

Fig. 2. Plot of $C^{1/3}$ vs. the crack length.

The mode mixity angle, Ψ, is defined as

$$\Psi = \tan^{-1}(\sqrt{G_{II}/G_I}). \tag{3.4}$$

Five, three and two specimens were tested, respectively, in mode I, mode II and mixed mode loadings. (Though testing additional specimens could have provided more confidence in the results obtained, results for each group of specimens ranged from $\pm$10% to $\pm$14%, which was deemed to be typical of fracture results.) Cracks in the adhesive propagated stably in all of these specimens. From experimental values of F_I, F_{II} and a, fracture energy values at different mode mixity angles were calculated from Eqs. (3.2–3.4). Experimental and computational results are discussed in Sections 5 and 6.

4. Verification of the codes for numerical simulation

4.1. Verification of the code by the method of manufactured solutions

The method of manufactured solutions [23,24] is used to verify the in-house developed code. Consider plane strain deformations of a cantilever-like beam of length L = 10 mm and H = 1.0 mm, and made of a homogeneous and isotropic linear elastic material having E = 1.0 MPa, and $\upsilon = 0.3$. We arbitrarily choose the following displacement field (any other smooth displacement field will be fine too):

$$u_1 = -0.01\left(x_2 - \frac{H}{2}\right)[3x_1(2L - x_1) + x_2(x_2 - H)]e^{x_1/10L},$$
$$u_2 = 0.005\left[x_1^2(3L - x_1) + (L - x_1)\left(x_2 - \frac{H}{2}\right)^2 + H^2 x_1\right]e^{x_1/10L}. \tag{4.1}$$

Note that for the displacement field (4.1) u_1 and u_2 vanish only at the point (0, H/2) and not on the entire edge $x_1 = 0$. Furthermore, stresses derived from Eq. (4.1) and Hooke's law do not give null tangential tractions on the top and the bottom surfaces of the beam. Using these displacements we find the stress field from Eqs. (A.24) and (A.26) and the body force from Eq. (A.18) required to satisfy the balance of linear momentum. With surface tractions on the top, bottom and right surfaces found from the stress field, essential boundary conditions on the left surface and computed values of body force as input into the code, the problem is numerically solved with the developed code. The computed displacements and stresses are compared with the assumed analytical displacements defined by Eq. (4.1) and stresses derived from them.

For generating SSPH basis functions, the Gauss weight function and the radius of the compact support of the weight function associated with a particle equal to four times the smallest distance of the particle from its nearest neighbor and complete polynomials of degree two for generating SSPH basis functions were found to give reasonably accurate results in [15] and are used in this work. Integrals on Ω appearing in Eq. (A.29) are evaluated by using the 9×9 Gauss integration rule and those on Γ by employing the 9 Gauss point integration rule. Three different particle distributions placed in uniform rectangular grids of 11×9, 21×9 and 21×11 are used for analyzing the boundary-value problem described above.

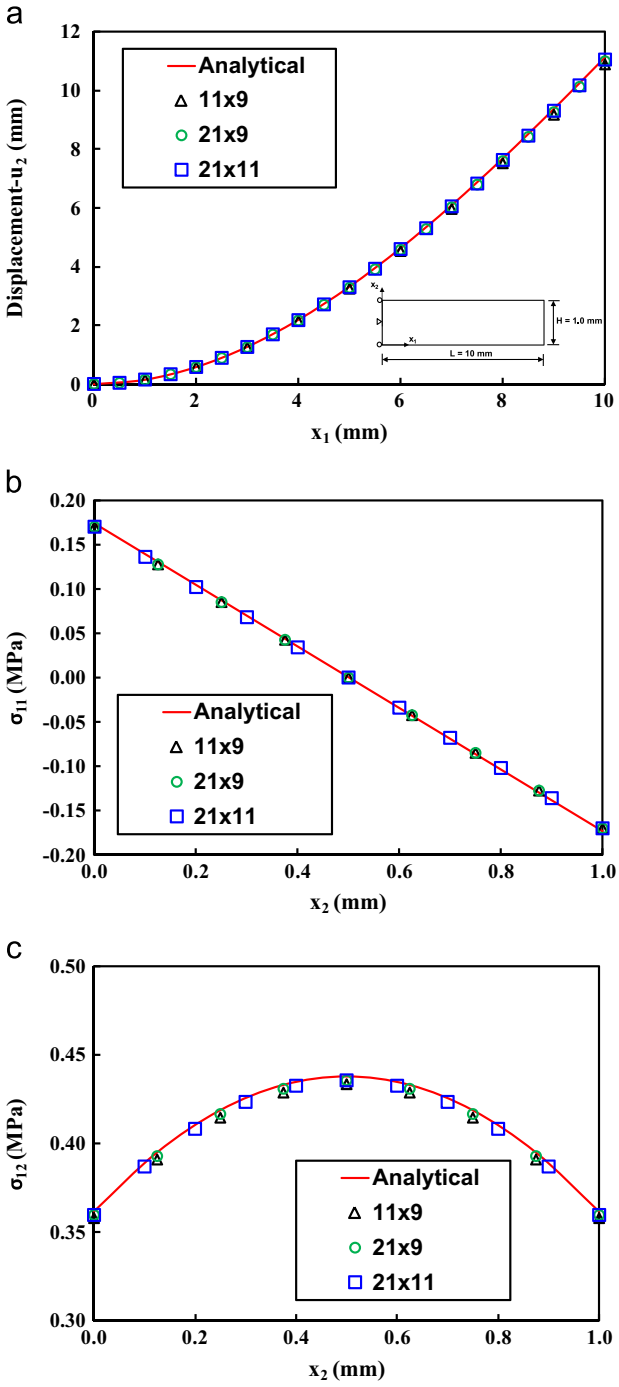

Fig. 3. Comparison of numerical and analytical solutions for (a) displacement u_2 along the line $x_2 = $H/2, and stress components (b) σ_{11}, and (c) σ_{12} along the line $x_1 = L/2$.

The computed displacement and stress fields are compared with the corresponding analytical ones in Fig. 3. It is clear that the converged numerical results agree well with the corresponding analytical solutions.

4.2. Verification of implementation of the CZM

In order to verify that the CZM has been accurately implemented in the computer code, we have analyzed a rather simple

problem schematically depicted in Fig. 4. Two flat adherend beams bonded together with an adhesive layer and subjected to normal and tangential loads are assumed to undergo plane strain deformations by applying surface tractions to their bounding surfaces as shown in Fig. 4. Values of material parameters are $E=1$ TPa (3 GPa), $\nu=0.33$ (0.3) for the adherend (adhesive). The CZM parameters for mode I and mode II are: initial stiffness=1 GPa/mm and critical stress=5 MPa, $G_{Ic}=0.05$ J/m^2, $G_{IIc}=0.1$ J/m^2. Thus adherends are assumed to be essentially rigid to focus on the predictions of the CZM model. Boundary conditions are: the bottom surface is rigidly clamped and displacements, δ_n and δ_t, are applied on the top surface for normal and tangential loading conditions, respectively.

Uniformly distributed 200×200 and 1000×50 particles are placed in each adherend and the adhesive, respectively, and the distance between adjacent particles on the cohesive segment is 0.01 mm. Computed reactions per unit surface area of the cohesive segment against the relative displacements for mode I deformations are compared in Fig. 5 with the corresponding analytical values. Similar results obtained for mode II deformations are not shown here. It is clear that the two sets of values agree well with each other; the maximum relative errors are 0.0041% and 0.0063% for mode I and mode II deformations, respectively.

4.3. Comparison of computed and experimental results for mode I loading

A schematic sketch of the plane strain problem studied is shown in Fig. 1 and the specimen is loaded by incrementing $\delta_1=\delta_2$. We analyze the problem experimentally studied by Pirondi et al. [25] and numerically by Alfano et al. [26] using the FEM in order to show that the SSPH method gives results identical to those given by the FEM; the fracture parameters assumed for this problem are taken from their work. We set $L=120$ mm, $H/2=10$ mm and the starter crack length $a=40$ mm, $E=70$ GPa,

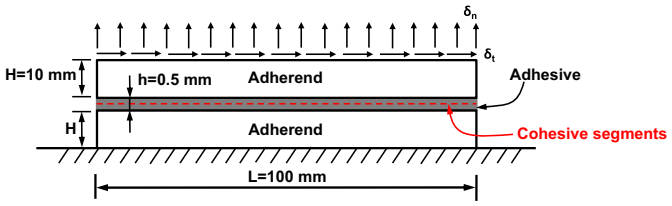

Fig. 4. Schematic sketch of the DCB problem analyzed to verify implementation of the CZM.

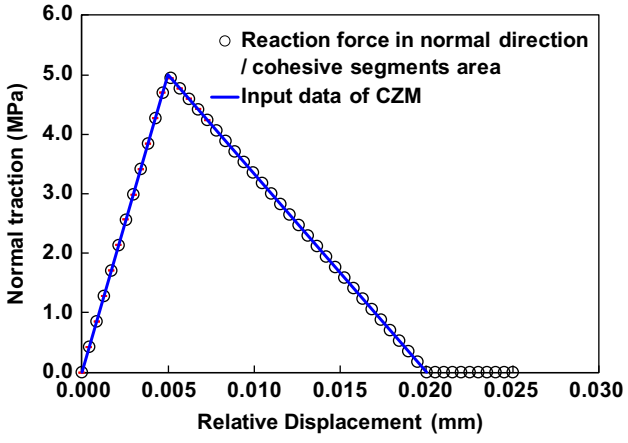

Fig. 5. Comparison of the computed reaction force in the normal direction divided by the cohesive segments area vs. the displacement of the top surface with the input value.

and $\upsilon=0.30$ for the adherend material. Values assigned to the CZM parameters are the same as those used in [26]; i.e., fracture energy $G_{Ic}=550\,J/m^2$ and critical cohesive stress $\tau_{cr}^{I}=3.5$ MPa. The effect of adhesive thickness is neglected in the simulations, i.e., the two adherends are tied together and the cohesive zone segments are placed at the interface. For particles uniformly distributed in the domain, d_x and d_y equaling the distance between adjacent particles in the adherends along x and y directions, respectively, and d_{xc} equal to the distance between adjacent particles on the interface between the two adherends, results were computed for $(d_x,d_y,d_{xc})=(1,1,0.1)$, $(0.5,1,0.05)$, $(0.5,1,0.010)$. For three different particle distributions the computed load–displacement curves (not shown here) overlapped each other signifying that computed results are essentially the same for the three particle distributions.

In Fig. 6, the presently computed load–displacement curve for particle distribution 3 is compared with that obtained experimentally by Pirondi et al. [25] and also with that computed by Alfano et al. [26] using the FEM. It can be observed that the presently computed results are very close to the experimental ones and also agree well with those of Alfano et al. Differences in the two numerically predicted peak loads and the experimental one of 1290 N are 3.1% and 6.7% for the meshless and the FE methods, respectively. Differences in the crosshead displacement at which peak loads occur are 8.8% and 2.9% for the meshless and the FE methods. Since Alfano et al. [26] did not report that their results are fully converged with respect to the FE mesh used, it is difficult to pin point reasons for differences between numerical results obtained by the FE and the SSPH methods.

5. Determination of optimum values of CZM parameters

5.1. Mode I deformations

Recalling that values of the peak surface traction τ_{cr}^{I} and the initial stiffness K_0^I of the traction–separation relation in the CZM affect computed results whereas the area under the traction–separation curve is fixed by the experimental value of the critical SERR, we now describe an algorithm for finding optimum values of τ_{cr}^{I}. We note that the area under the traction–separation relation (i.e., the critical SERR) is determined from the test data and is a material dependent property. Thus it is not used when finding optimum values of parameters for the CZM. We analyze the plane strain boundary value problem for the DCB specimen tested in our laboratory. Values of material properties for the adherend and the adhesive layer taken from manufacturer's website are: $E=70$ GPa and $\upsilon=0.33$ for the adherend; $E=3.0$ GPa, and $\upsilon=0.30$ for the adhesive. The value of mode I fracture energy, G_{Ic}, found from

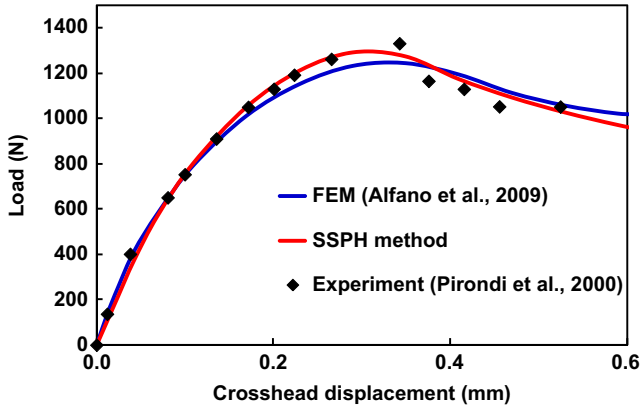

Fig. 6. Comparison of the numerically computed and the experimentally observed load vs. displacement curves.

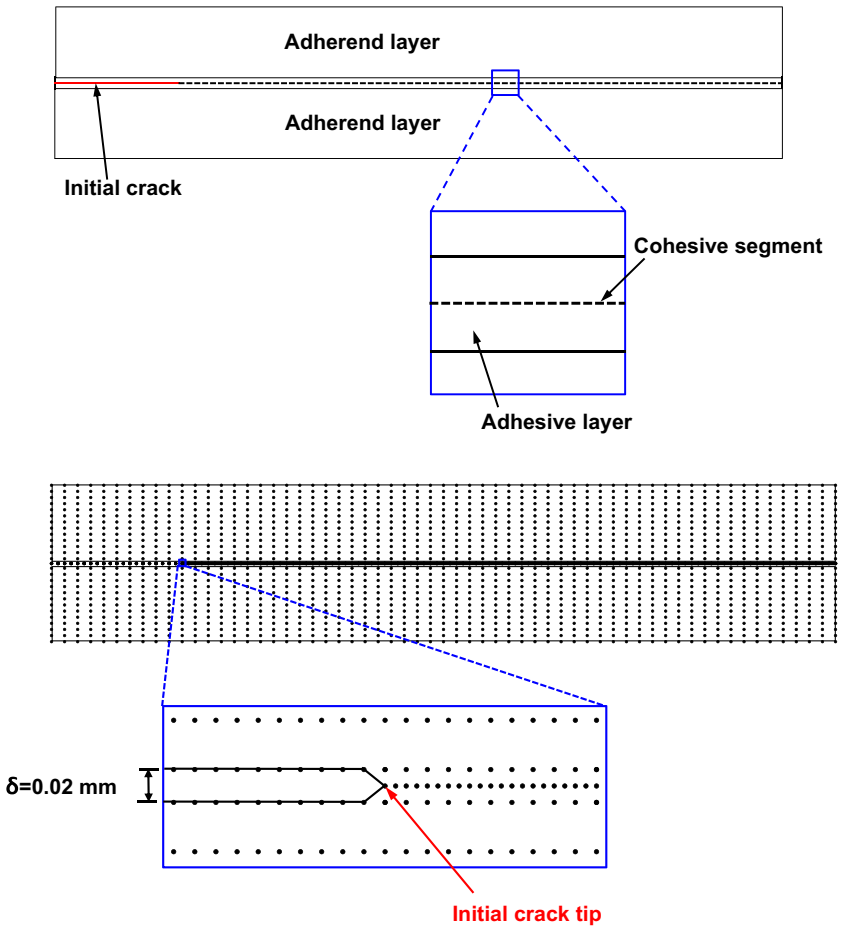

Fig. 7. Distribution of particles in the DCB specimen and the geometry of the initial crack.

Table 2
Values in mm of d_x, d_y in the adherend and the adhesive and d_x in the cohesive segment.

Particle distribution	Adherend	Adhesive	Cohesive segment
1	4, 2	0.10, 0.10	0.10
2	2, 1	0.05, 0.05	0.05
3	2, 1	0.02, 0.03	0.01

Eq. (3.2) and the experimental data is 466.3 J/m^2. As was done in experiments, the specimen is deformed by prescribing the vertical displacement, δ_1 and δ_2, on the top and the bottom adherends, respectively. Although not shown, plots of G_{Ic} from all the five specimens vs. crack length were relatively flat and the variation is within $\pm$10% of the mean value used herein.

The distribution of particles and the geometry of the initial crack tip with initial crack opening displacement of 0.02 mm are exhibited in Fig. 7. The conical crack-tip exhibited in Fig. 7 is an artifact of joining adjacent particles by straight lines. In the SSPH formulation, particles are not connected with each other, thus the crack-tip is not as sharp as that exhibited in Fig. 7. Results are computed for three particle distributions listed in Table 2.

The central composite design technique described in [27] is used to find optimal values of the cohesive parameters in the CZM by assuming a second order relation (a complete polynomial of degree 2).

$$Y=\beta_0+\beta_1X_1+\beta_2X_2+\beta_3X_1^2+\beta_4X_2^2+\beta_5X_1X_2, \tag{5.1}$$

where coefficients β_0, $\beta_1 \ldots \beta_5$ are to be determined, and X_i is the design variable and Y is the objective function. We take

$$Y=\lambda\tilde{E}_f+(1-\lambda)\tilde{E}_p$$
$$=\lambda\left(\sqrt{\sum_{i=1}^{n}((f^i_{\exp}-f^i_{num}))^2}\Big/\sqrt{\sum_{i=1}^{n}(f^i_{\exp})^2}\right)+(1-\lambda)\left|\frac{(P_{\exp}-P_{num})}{P_{\exp}}\right| \tag{5.2}$$

where f is the load at a given displacement, P is the maximum load, n equals the number of values of displacements where the load is evaluated, and λ, $0\le\lambda\le1$, is the weight assigned to $\tilde{E}_f$ in Eq. (5.2). Subscripts "exp" and "num" on f denote its values from the experimental data and the numerical results, respectively. The objective function, Y, is composed of two parts: the relative difference in the experimental and the computed values of loads for n values of displacements, $\tilde{E}_f$, and the relative difference in peak values of the experimental and the computed loads, $\tilde{E}_p$, as shown in Fig. 8.

For $n=100$, computed values of CZM parameters for $\lambda=0$, 0.5 and 1 are listed in Table 3. For $\lambda=0.5$, we have given in Table 4 values of $\tilde{E}_f$ and $\tilde{E}_p$ for mode I loading with three different particle distributions listed in Table 2. As expected values of $\tilde{E}_f$ and $\tilde{E}_p$ decrease monotonically with a decrease in the distance between adjacent particles in x and y directions. For $\lambda=0$, 0.5 and 1, the computed load–displacement curves are compared with the experimental ones for pure mode I loading in Fig. 9. For $\lambda=0$, 0.5 and 1, differences in the computed and the experimental peak loads equal, respectively, 0.9%, 1.24% and 5.21%. Thus the error in the computed peak load can be minimized by setting $\lambda=0$. However, then the error in the computed and the experimental peak loads for mixed mode deformations may not be minimized.

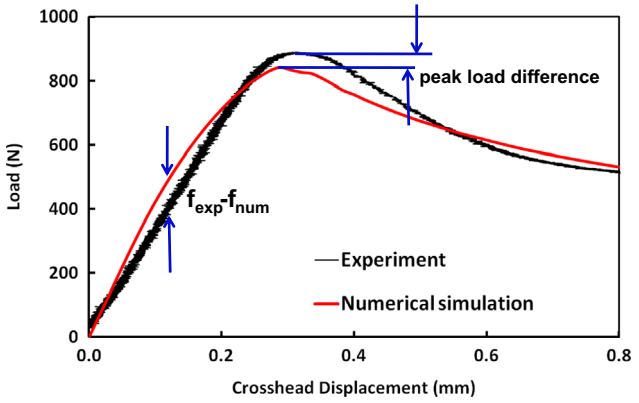

Fig. 8. The load–displacement curves for experimental and simulation results for mode I loading.

Table 3
For λ=0, 0.5 and 1.0, optimum values of the CZM parameters for mode I deformations.

λ	τ_{cr}^{I} (MPa)	K_0^I (MPa/mm)
0.0	10.8	3058
0.5	11.6	2940
1.0	9.2	3024

Table 4
For three different particle distributions, values of $\tilde{E}_f$ and $\tilde{E}_p$ for mode I loading.

Particle distribution	$\tilde{E}_f$	$\tilde{E}_p$
1	0.116	0.018
2	0.108	0.015
3	0.103	0.012

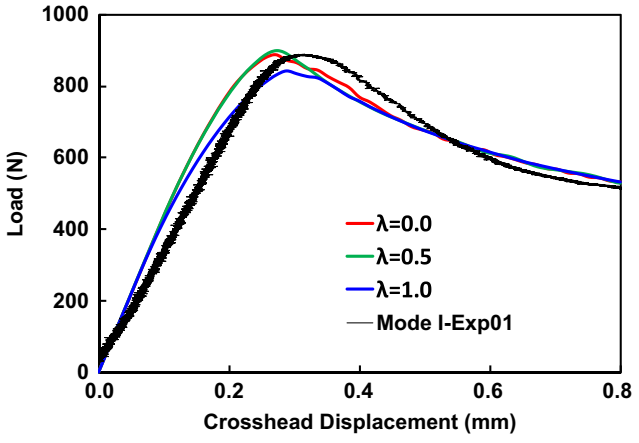

Fig. 9. For three values of the weight λ, load vs. displacement curves for pure mode I loading.

We suggest that one take λ=0.5. For λ=0.5, the response surface, i.e., Y as a function of the critical cohesive stress and the initial interface stiffness, is shown in Fig. 10. The function has the minimum value when $\tau_{cr}^{I}=11.6$ MPa, $K_0^I=2940$ MPa/mm for mode I deformations.

5.2. Mode II deformations

The approach outlined in subsection 5.1 to find optimum values of τ_{cr}^{II} and K_0^{II} gave inappropriate values of these variables. We set

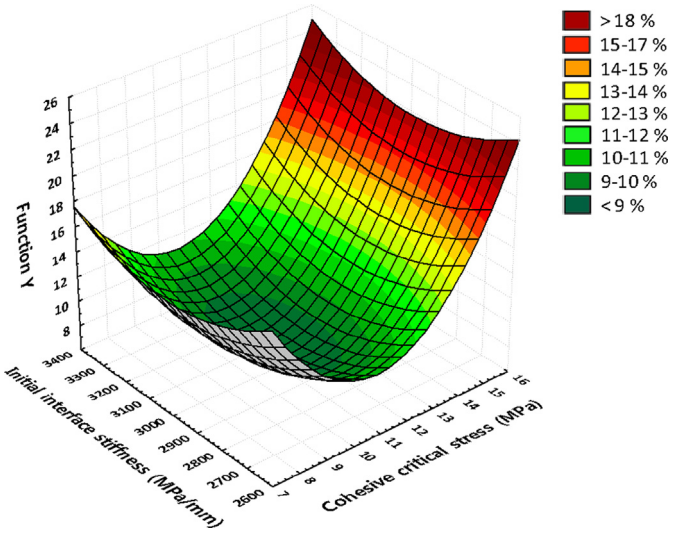

Fig. 10. Variation of the objective function Y with the critical cohesive stress and the initial interface stiffness for mode I loading.

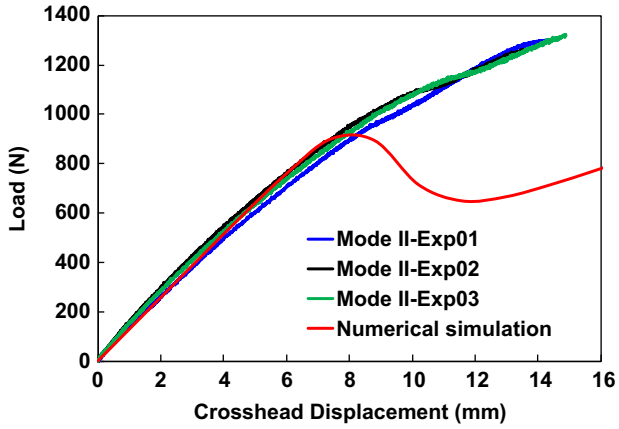

Fig. 11. Experimental and numerical computed load vs. displacement curves for mode II loading.

$K_0^{II}=1105$ MPa/mm which equals the adhesive shear modulus/adhesive thickness, and found $\tau_{cr}^{II}=40.0$ MPa by minimizing $\tilde{E}_f$ for the nearly linear part of load–displacement curves. The best fit traction value in shear is considerably higher than that obtained for mode I, a somewhat surprising result if these terms were directly related to yield phenomenon, though others have shown poor correlations of these fitted peak tractions with other physical properties [32]. Recognizing the much higher fracture energy in shear and the noted susceptibility of adhesive bonds to peel stresses, this difference may be appropriate. $G_{IIc}=1897\ N/m$ is found by averaging the values found by using Eq. (3.3) and the data for the three tests. For these values of τ_{cr}^{II} and K_0^{II} the computed load–displacement curve is compared with the experimental ones in Fig. 11. In the experimental results, the load monotonically increases whereas in numerical simulations it attains a peak value. These differences could be due to (i) the poor reproducibility of test values of G_{IIc} [28], (ii) neglecting in the numerical work friction at the crack surfaces, (iii) the adhesive stress–strain curve not obeying Hooke's law, (iv) the adhesive not being a homogeneous material, and (v) damage mechanisms such as the initiation and propagation of inclined microcracks [29] not considered in the mathematical model. We note that Ameli et al. [30] used the FEM to study the plastic zone evolution with crack growth.

6. Comparison of numerical and test results for mode I and mixed mode deformations

6.1. Mode I deformations

Three DCB specimens with the same geometry as that mentioned in Subsection 5.1, but different crack length $a=80$ mm, were tested in mode I loading. The numerically predicted load–displacement curves using the optimal mode I CZM parameters are shown in Fig. 12 along with the experimental ones. It is evident that for all three tests there is good agreement between numerical and experimental results with the maximum difference between the computed and the measured peak loads less than 7.0%. In Fig. 13, we have compared the computed load vs. the crack length with the corresponding experimental results. The close agreement between the two sets of results implies that the failure behavior of the DCB specimen under mode I loading is accurately described by the proposed mathematical and computational model. The variation with the crack length of the computed T-stress at the point 0.01 mm away from the crack tip [15,30] exhibited in Fig. 14 reveals that the T-stress increases as the crack propagates. Negative values of the T-stress imply stable crack growth as observed in experiments.

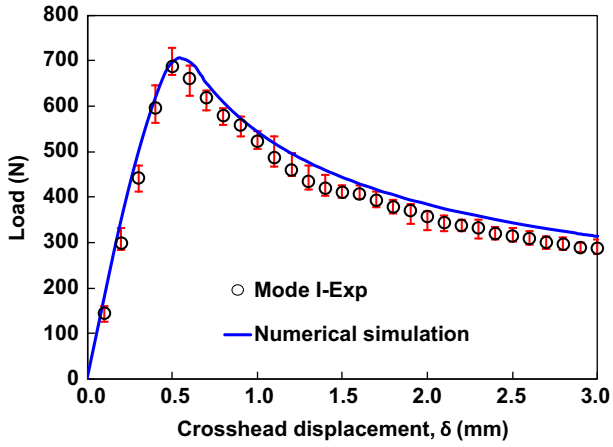

Fig. 12. Comparison of the computed and experimental (3 specimens) load–displacement curves under mode I loading.

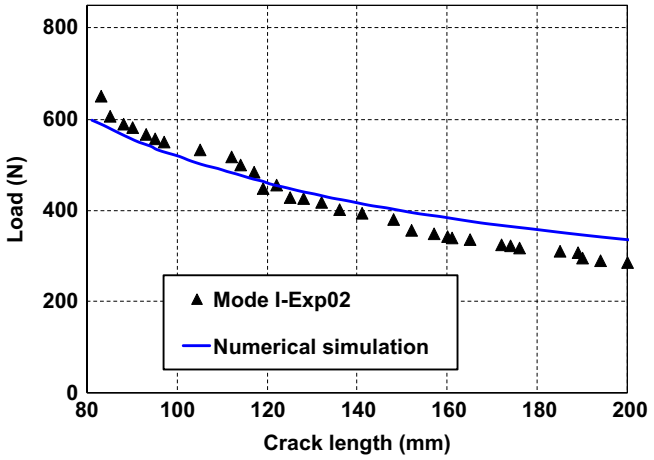

Fig. 13. Comparison of the computed and the experimental load vs. crack length for the DCB specimen under mode I loading.

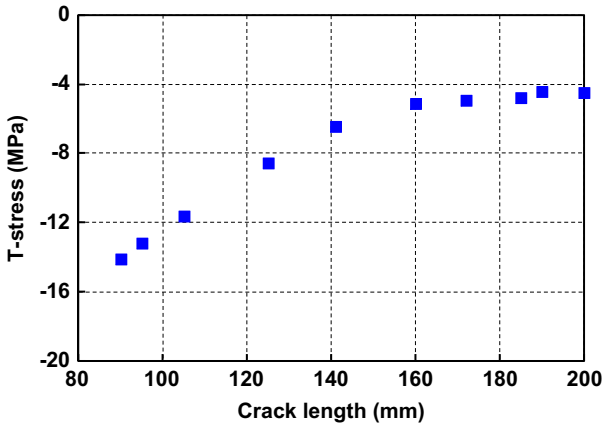

Fig. 14. For mode I deformations of the DCB specimen variation of the computed T-stress with the crack length.

Table 5
Values of the initial crack length and the displacement ratio R for DCB specimens deformed under mixed mode loading.

Experiment	Initial crack length (mm)	R	Mode mixity angle range (degree)
MM-Exp01	80	−2.0	20–40
MM-Exp02	130	−2.0	35–55
MM-Exp03	80	−1.3	50–75

6.2. Mixed mode deformations

Three DCB specimens were tested under mixed mode loading with the applied displacement ratio $R=\Delta\delta_1/\Delta\delta_2$ where $\Delta\delta_1$ and $\Delta\delta_2$ equal increments in δ_1 and δ_2, respectively. Using Eqs. (3.2–3.4), we find that the mode mixity angle, Ψ, varies approximately from 20° to 75° as the crack propagates; e.g. see Table 5.

The experimental and the computed load–displacement curves for the top adherend are compared in Fig. 15. It is clear that the computed peak failure load agrees well with the experimental one with the largest relative error in the peak load of 2.8%. However, subsequent to the peak load, the difference between the numerical and the experimental loads increases with an increase in the mode mixity angle. Using Eq. (A.14), the total fracture energy can be expressed as

$$G_{total}=G_I+G_{II}=[(1-\alpha)/G_{Ic}+(\alpha)/G_{IIc}]^{-1}, \tag{6.1}$$

where $\alpha=\tan^2(\Psi)/[1+\tan^2(\Psi)]$.

Fig. 16 shows the experimental discrete data of the total fracture energy versus the mode mixity angle, Ψ, and the plot of Eq. (6.1). In the range of $15^\circ<\Psi<55^\circ$, the failure criterion (A.14) (or Eq. (6.1)) successfully describes the experimental observations. For $55^\circ<\Psi<80^\circ$, deviations between values from Eq. (A.14) and the experimental data increase rapidly with an increase in Ψ. Thus, for the adhesive studied herein, the failure criterion given by Eq. (A.14) can be successfully applied to simulate the failure behavior of the DCB specimen for $\Psi<55^\circ$. Since the values of fracture energy increase with the growth of crack length in tests with high mode mixity angles, this model underestimates the fracture energy for $\Psi>55^\circ$. Attempts to increase the value of G_{IIc}, though producing better agreement at large mode mixity angles, resulted in poorer fit at intermediate angles, where we have the greatest confidence in the experimental data. Obtaining meaningful mode II fracture energies for tougher adhesives is complicated by the large plastic zones that may be induced, as recently noted by Blackman et al. [33], so less emphasis has been placed on obtaining model agreement for large mode mixity angles.

The computed T-stress and the mode mixity angle plotted in Fig. 17 against the crack length suggest that that the value of the

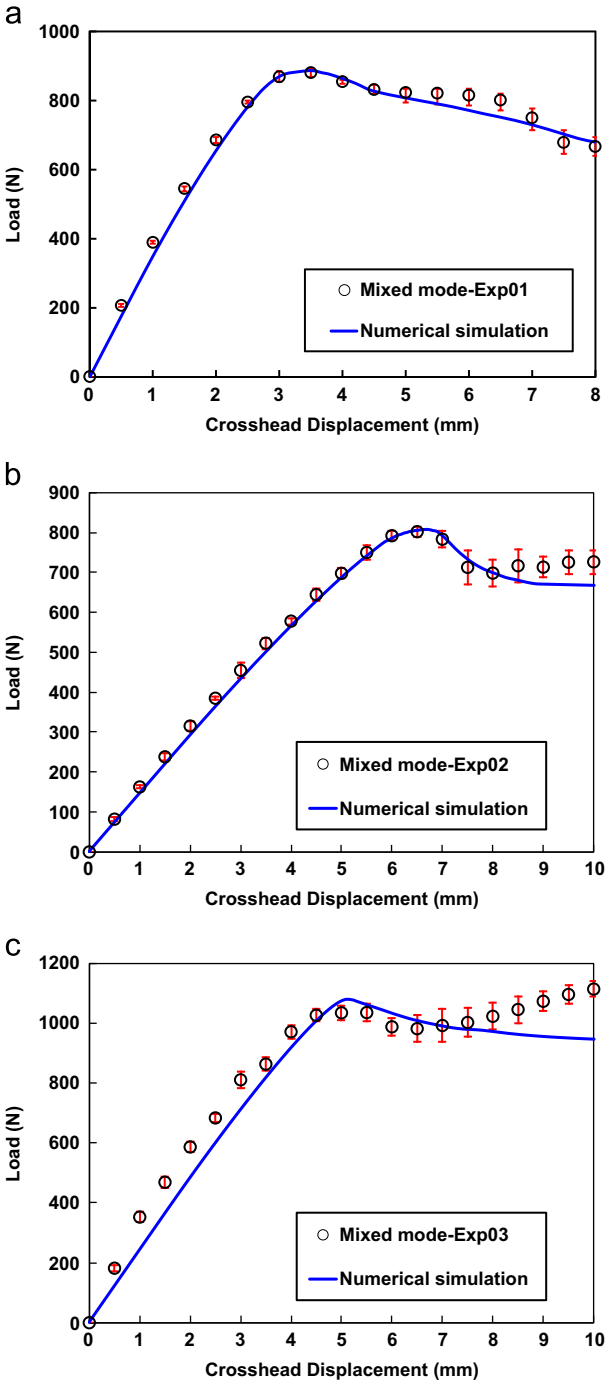

Fig. 15. Experimental and numerically computed load–displacement curves for the top adherend for (a) $R=-2$, initial crack length=80 mm, (b) $R=-2$, initial crack length=130 mm, and (c) $R=-1.3$, initial crack length=80 mm.

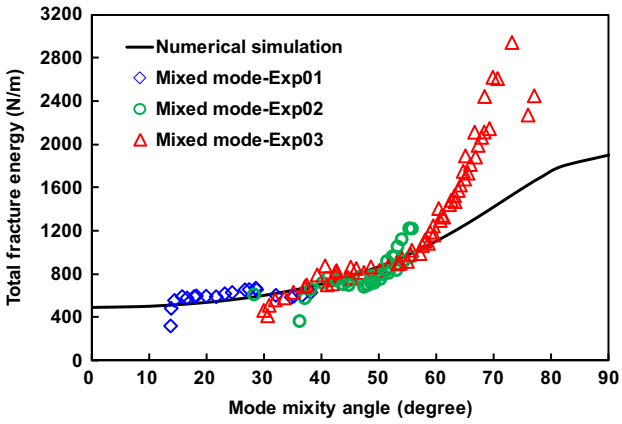

Fig. 16. Variation of the total fracture energy with the mode mixity angle.

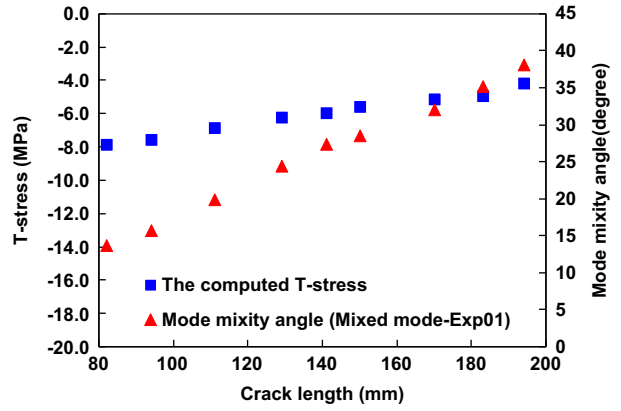

Fig. 17. Variation with the crack length of the computed T-stress and the mode mixity angle for the DCB specimen.

T-stress increases with an increase in the mode mixity angle implying that the crack may become unstable for large values of Ψ.

7. Conclusions

We have computationally and experimentally studied static deformations of DCB specimens under mode I, mode II and mixed mode loading. The experimental work has employed a unique dual force actuator that enables continuous variation of the mode-mixity angle. The computational work based on meshless method has used symmetric smooth particle hydrodynamics (SSPH) basis functions. A jump function has been used to ensure continuity of surface tractions across an interface between two different materials, and the CZM has been implemented to simulate crack initiation and propagation. The developed software has been verified by the method of manufactured solutions. Values of the CZM parameters for mode I deformations have been determined through a composite design technique that minimizes an objective function.

The computed load–displacement curves for DCB specimens deformed in mode I have been found to agree well with the corresponding test findings with the maximum difference between the computed and the experimental peak loads being less than 7%. Furthermore, computed values of the T-stress ahead of the crack tip imply stable crack growth which is consistent with test results.

For mode II deformations the strain energy release rate (SERR) found from experimental results increases with an increase in the crack length. However, in computational work we have used a constant value of the critical SERR. The computed results for mixed mode deformations have been found to be close to the corresponding experimental ones only for the mode mixity angle less than 50°. Computed values of the T-stress monotonically increase with an increase in the mode mixity angle implying that a crack may become unstable for high values of the mode mixity angle.

Acknowledgments

The authors gratefully acknowledge the financial support of the National Science Foundation through NSF/CMMI Award no. 0826143, as well as their support under DMR-0415840 for the construction of the dual actuator load frame used in this research. In addition, we acknowledge use of facilities in the Engineering Science and Mechanics and Chemistry Departments, as well as the Macromolecules and Interfaces Institute for fostering interdisciplinary research.

Appendix

A.1 Symmetric smoothed particle hydrodynamics (SSPH) basis functions

The value of function $f(\mathbf{x})$ having continuous derivatives up to $(m+1)$ order at a point $\boldsymbol{\xi}=(\xi_1,\xi_2,\xi_3)$ in the domain of definition of $f(\mathbf{x})$ can be approximated in terms of values of $f(\mathbf{x})$ and of its derivatives at the point $\mathbf{x}=(x_1,x_2,x_3)$ by the following finite Taylor series:

$$f(\boldsymbol{\xi})=\sum_{k=0}^{m}\frac{1}{k!}\left[(\xi_1-x_1)\frac{\partial}{\partial x_1}+(\xi_2-x_2)\frac{\partial}{\partial x_2}+(\xi_3-x_3)\frac{\partial}{\partial x_3}\right]^k f(\mathbf{x}). \tag{A.1}$$

Eq. (A.1) can be viewed as expressing $f(\boldsymbol{\xi})$ in terms of complete polynomials of order m in $\boldsymbol{\xi}$. Here we set $m=2$, and rewrite Eq. (A.1) in terms of matrices $\mathrm{P}(\boldsymbol{\xi},\mathbf{x})$ and $\mathrm{Q}(\mathbf{x})$ as

$$f(\boldsymbol{\xi})=\mathrm{P}(\boldsymbol{\xi},\mathbf{x})\mathrm{Q}(\mathbf{x}), \tag{A.2}$$

where

$$\mathrm{P}(\boldsymbol{\xi},\mathbf{x})=[1,\xi_1-x_1,\xi_2-x_2,\xi_3-x_3,(\xi_1-x_1)^2,(\xi_2-x_2)^2,(\xi_3-x_3)^2,(\xi_1-x_1)(\xi_2-x_2),(\xi_2-x_2)(\xi_3-x_3),(\xi_3-x_3)(\xi_1-x_1)],$$

$$\mathrm{Q}(\mathbf{x})=[f(\mathbf{x}),\frac{\partial f(\mathbf{x})}{\partial x_1},\frac{\partial f(\mathbf{x})}{\partial x_2},\frac{\partial f(\mathbf{x})}{\partial x_3},\frac{1}{2}\frac{\partial^2 f(\mathbf{x})}{\partial x_1^2},\frac{1}{2}\frac{\partial^2 f(\mathbf{x})}{\partial x_2^2},\frac{1}{2}\frac{\partial^2 f(\mathbf{x})}{\partial x_3^2},\frac{\partial^2 f(\mathbf{x})}{\partial x_1\partial x_2},\frac{\partial^2 f(\mathbf{x})}{\partial x_2\partial x_3},\frac{\partial^2 f(\mathbf{x})}{\partial x_3\partial x_1}].$$

Elements of matrix $\mathrm{Q}(\mathbf{x})$, i.e., the function $f(\mathbf{x})$ as well as its first and second derivatives, are unknowns to be found. Elements of matrix $\mathrm{P}(\boldsymbol{\xi},\mathbf{x})$ are known and are complete polynomials of degree 2. In order to find elements of matrix $\mathrm{Q}(\mathbf{x})$, we premultiply both sides of Eq. (A.2) with $W(\boldsymbol{\xi},\mathbf{x})\mathrm{P}(\boldsymbol{\xi},\mathbf{x})^T$ and obtain

$$\begin{aligned}W(\boldsymbol{\xi},\mathbf{x})\mathrm{P}^T(\boldsymbol{\xi},\mathbf{x})f(\boldsymbol{\xi})&=W(\boldsymbol{\xi},\mathbf{x})\mathrm{P}^T(\boldsymbol{\xi},\mathbf{x})\mathrm{P}(\boldsymbol{\xi},\mathbf{x})\mathrm{Q}(\mathbf{x}),\\&=[\mathrm{P}^T(\boldsymbol{\xi},\mathbf{x})W(\boldsymbol{\xi},\mathbf{x})\mathrm{P}(\boldsymbol{\xi},\mathbf{x})]\mathrm{Q}(\mathbf{x}),\end{aligned} \tag{A.3}$$

where $W(\boldsymbol{\xi},\mathbf{x})$ is a weight function of compact support associated with particle $\mathbf{x}$ as shown in Fig. A1. Let there be $N(\mathbf{x})$ particles in the compact support of $W(\boldsymbol{\xi},\mathbf{x})$. Eq. (A.3) is evaluated at every particle I in the compact support of $W(\boldsymbol{\xi},\mathbf{x})$, and summed to obtain

$$\sum_{I=1}^{N(\mathbf{x})}f(\boldsymbol{\xi}^{\mathrm{I}})W(\boldsymbol{\xi}^{\mathrm{I}},\mathbf{x})\mathrm{P}(\boldsymbol{\xi}^{\mathrm{I}},\mathbf{x})=\sum_{I=1}^{N(\mathbf{x})}[\mathrm{P}^T(\boldsymbol{\xi}^{\mathrm{I}},\mathbf{x})W(\boldsymbol{\xi}^{\mathrm{I}},\mathbf{x})\mathrm{P}(\boldsymbol{\xi}^{\mathrm{I}},\mathbf{x})]\mathrm{Q}(\mathbf{x}), \tag{A.4}$$

where $\boldsymbol{\xi}^{\mathrm{I}}$ denotes coordinates of the I^{th} particle. We set

$$\mathrm{H}(\boldsymbol{\xi},\mathbf{x})=[\mathrm{P}^T(\boldsymbol{\xi}^1,\mathbf{x}),\mathrm{P}^T(\boldsymbol{\xi}^2,\mathbf{x}),\ldots,\mathrm{P}^T(\boldsymbol{\xi}^{N(\mathbf{x})},\mathbf{x})],$$

$$\mathrm{W}(\boldsymbol{\xi},\mathbf{x})=\begin{bmatrix}W(\boldsymbol{\xi}^1,\mathbf{x}) & 0 & \cdots & 0\\ 0 & W(\boldsymbol{\xi}^2,\mathbf{x}) & \cdots & \vdots\\ \vdots & 0 & \ddots & 0\\ 0 & 0 & \cdots & W(\boldsymbol{\xi}^{N(\mathbf{x})},\mathbf{x})\end{bmatrix},$$

$$\mathrm{F}^T(\boldsymbol{\xi})=[f(\boldsymbol{\xi}^1),f(\boldsymbol{\xi}^2),\ldots,f(\boldsymbol{\xi}^{N(\mathbf{x})})].$$

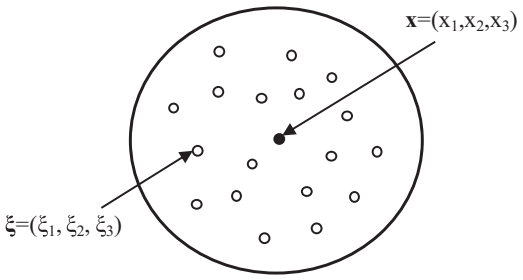

Fig. A1. Distribution of particles in the compact support of $W(\boldsymbol{\xi},\mathbf{x})$ associated with point $\mathbf{x}$.

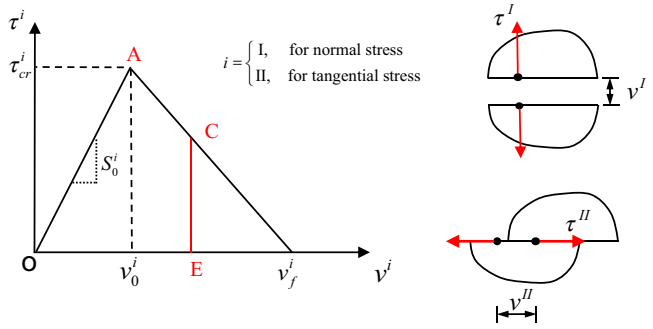

Fig. A2. Traction–separation law used for the CZM.

Thus, Eq. (A.4) can be written as

$$\mathrm{C}(\boldsymbol{\xi},\mathbf{x})\mathrm{Q}(\mathbf{x})=\mathrm{D}(\boldsymbol{\xi},\mathbf{x})\mathrm{F}(\boldsymbol{\xi}), \tag{A.5}$$

where

$$\mathrm{C}(\boldsymbol{\xi},\mathbf{x})=\mathrm{H}(\boldsymbol{\xi},\mathbf{x})\mathrm{W}(\boldsymbol{\xi},\mathbf{x})\mathrm{H}^T(\boldsymbol{\xi},\mathbf{x}),\ \mathrm{D}(\boldsymbol{\xi},\mathbf{x})=\mathrm{H}(\boldsymbol{\xi},\mathbf{x})\mathrm{W}(\boldsymbol{\xi},\mathbf{x}). \tag{A.6}$$

In Eqs. (A.5) and (A.6), values of elements of matrices $\mathrm{H}(\boldsymbol{\xi},\mathbf{x})$, $\mathrm{W}(\boldsymbol{\xi},\mathbf{x})$ and $\mathrm{F}(\boldsymbol{\xi})$ depend upon coordinates, the weight function, and on values of the function $f(\boldsymbol{x})$ at all particles in the compact support of $W(\boldsymbol{\xi},\mathbf{x})$. Thus $\mathrm{Q}(\mathbf{x})$ can be found from Eq. (A.5) by inverting $\mathrm{C}(\boldsymbol{\xi},\mathbf{x})$. That is,

$$\mathrm{Q}(\mathbf{x})=\mathrm{K}(\boldsymbol{\xi},\mathbf{x})\mathrm{F}(\boldsymbol{\xi}), \tag{A.7}$$

where $\mathrm{K}(\boldsymbol{\xi},\mathbf{x})=[\mathrm{C}(\boldsymbol{\xi},\mathbf{x})]^{-1}\mathrm{D}(\boldsymbol{\xi},\mathbf{x})$. The sufficient condition for matrix $\mathrm{C}(\boldsymbol{\xi},\mathbf{x})$ to be invertible is that the number, $N(\mathbf{x})$, of particles in the compact support of $W(\boldsymbol{\xi},\mathbf{x})$ be at least equal to the number of unknowns in matrix $\mathrm{Q}(\mathbf{x})$. The first two rows and the fifth row of elements of the matrix $\mathrm{Q}(\mathbf{x})$ can be written explicitly as

$$f(\mathrm{x})=\sum_{i=1}^{N(\mathbf{x})}K_{1i}F_i,\frac{\partial f(\mathbf{x})}{\partial x_1}=\sum_{i=1}^{N(\mathbf{x})}K_{2i}F_i,\frac{\partial^2 f(\mathbf{x})}{\partial x_1^2}=\sum_{i=1}^{N(\mathbf{x})}2K_{5i}F_i. \tag{A.8}$$

In the FE terminology, functions K_{1i}, K_{2i} and $2K_{5i}$ are shape functions for $f(\mathbf{x})$, $\partial f(\mathbf{x})/\partial x_1$ and $\partial^2 f(\mathbf{x})/\partial x_1^2$, respectively. We note that $K_{2i}\neq\partial K_{1i}/\partial x_1$ and $2K_{5i}\neq\partial K_{2i}/\partial x_1$. That is, K_{2i} is not obtained by differentiating K_{1i} with respect to x_1.

A.2 Cohesive zone model (CZM)

The CZM model describes a traction–separation law which relates the cohesive stress $\boldsymbol{\tau}$ and the displacement jump $\boldsymbol{\nu}$ between abutting particles of the cohesive segment. Problems studied herein involve monotonic loading, and plane strain (2-D) deformations. Accordingly, we discuss the traction–separation relation only for monotonic loading. We assume this relation to be linear until the relevant stress component (i.e., either the normal stress, τ^I, or the tangential stress, τ^{II}) on the cohesive segment reaches its maximum value and subsequently an affine relation till this stress decreases to zero; e.g., see Fig. A2. For pure mode I and mode II

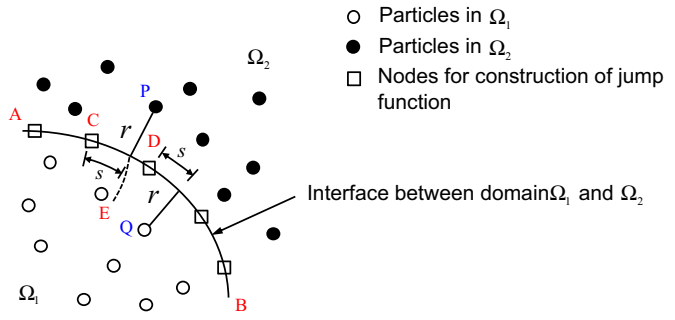

Fig. A3. Interface AB between domains Ω_1 and Ω_2 of different materials, particles in Ω_1 and Ω_2, and the definition of r.

deformations the traction–separation relation can be written as

$$\boldsymbol{\tau} = \mathbf{S}(\mathbf{v})\boldsymbol{v}, \tag{A.9}$$

where

$$\tau = \begin{bmatrix} \tau^I & 0 \\ 0 & \tau^{II} \end{bmatrix}, \boldsymbol{S} = \begin{bmatrix} S_0{}^I(\boldsymbol{v}^I) & 0 \\ 0 & S_0{}^{II}(\boldsymbol{v}^{II}) \end{bmatrix}, \boldsymbol{v} = \begin{bmatrix} v^I & 0 \\ 0 & v^{II} \end{bmatrix},$$

τ^i is the cohesive stress component and v^i is the relative displacement between initially abutting particles for mode $i (i = I, \text{II})$. $S^I(\boldsymbol{v}^I)$ and $S^{II}(\boldsymbol{v}^{II})$ are, respectively, the interface stiffnesses of modes I and II. It is postulated that the cohesive segment begins to weaken or the damage initiates when the jump in the appropriate component of displacements of the two adjoining points reaches the critical value, $v_0^i (i = I, \text{II})$. Subsequently, until the jump in v^i equals v_f^i, a softening law is assumed in the sense that the relative traction between the two surfaces affinely decreases with an increase in the relative displacement until it becomes zero for $v^i = v_f^i$ when the two layers either separate from or slide over each other. The relation between τ^i and v^i is expressed by piece-wise continuous functions listed in Eq. (A.10).

$$S_0^i(v^i) = \begin{cases} \frac{\tau_{cr}^i}{v_0^i}, & 0 \le v^i \le v_0^i, \\ \frac{\tau_{cr}^i}{v_0^i}\left(\frac{v_f^i/v^i - 1}{v_f^i/v_0^i - 1}\right) & v_0^i \le v^i \le v_f^i, \\ 0 & v^i > v_f^i. \end{cases} \tag{A.10}$$

For $v_0^i \le v^i \le v_f^i$, Eq. (A.10) can be written as

$$\tau^i = \frac{\tau_{cr}^i}{v_f^i - v_0^i}(v_f^i - v^i) \tag{A.11}$$

and is thus a polynomial of degree 1 in v^i.

The area under the entire traction–separation curve equals the critical fracture energy, i.e.,

$$G_{ic} = \frac{1}{2}\tau_{cr}^i v_f^i, \tag{A.12}$$

where τ_{cr}^i and $v_f^i (i = I, \text{II})$ are, respectively, the critical cohesive stress and the critical displacement jump, respectively, for mode I and mode II, and G_{Ic} and G_{IIc} are, respectively, the fracture energies for mode I and mode II.

For mixed mode loading, damage is assumed to initiate when the following criterion quadratic in stresses is satisfied [16].

$$\left(\frac{\tau^I}{\tau_{cr}^I}\right)^2 + \left(\frac{\tau^{II}}{\tau_{cr}^{II}}\right)^2 = 1, \quad \tau^I > 0. \tag{A.13}$$

If $\tau^I \le 0$ then there is no mode I and hence no mixed mode failure. We note that the separation between the two layers occurs only when the normal traction between the two contacting surfaces is tensile; otherwise one layer can slide over the other. Crack growth is simulated by using the following criterion between the energy release rates and their respective fracture energies:

$$\frac{\mathcal{G}_I}{G_{Ic}} + \frac{\mathcal{G}_{II}}{G_{IIc}} = 1, \quad \tau^I > 0. \tag{A.14}$$

For monotonically increasing values of v^i, $\mathcal{G}_I$ and $\mathcal{G}_{II}$ are given by Eq. (A.15). That is, the energy release rate in each mode equals the area under the corresponding traction–separation curve. When Eq. (A.14) is satisfied, the crack surfaces are assumed to have fully developed. For $\tau^I > 0$ preceding this instant, the adjoining surfaces separate from each other and τ^I and τ^{II} are set equal to zero.

$$\mathcal{G}_i = \begin{cases} \frac{1}{2}\tau^i v^i & v^i \le v_0^i \\ \frac{1}{2}[\tau_{cr}^i v_0^i + (\tau^i + \tau_{cr}^i)(v^i - v_0^i)] & v_0^i < v^i \le v_f^i \end{cases} \quad (i = I, \text{II}). \tag{A.15}$$

As mentioned above, problems analyzed in this work involve monotonic loading. Thus further discussion of computing $\mathcal{G}_I$ and $\mathcal{G}_{II}$for any value of τ^I and τ^{II} during unloading and reloading is not provided. For values of τ^I and τ^{II} corresponding to point C in Fig. A2,$\mathcal{G}_i$ equal area OACE.

We note that the above description of the CZM is with respect to local coordinates. Thus surface tractions and displacements will need to be converted from global to local coordinates and vice versa for proper implementation of the CZM.

A.3 Modeling discontinuity at the interface between two materials by using jump function

A characteristic of basis functions in a meshless method is that the trial solution and its spatial derivatives are generally continuous everywhere in the domain. Thus the satisfaction of continuity of surface tractions at the interface between two distinct materials of the body (e.g., a composite, a bonded joint) requires special treatment such as either the method of Lagrange multipliers or the introduction of a jump function [17] or a technique to generate discontinuous MLS basis function. For 1-D heat conduction and wave propagation problems, Batra et al. [18,34] have shown that these methods give essentially identical solutions. Here we introduce a jump function defined at points on the interface AB between two regions Ω_1 and Ω_2 composed of different materials; e.g., see Fig. A3. Particles in regions Ω_1 and Ω_2 are denoted by open and filled circles, respectively, and those on the interface AB by open squares. We denote the distance of a point from the interface by r as shown in Fig. A3, and approximate function f (e.g., a displacement component) at point P near the interface by

$$f(\mathbf{x}) = \sum_{i=1}^{N(\mathbf{x})} K_{1i}F_i + \left[\frac{s}{l}q_D + \left(1 - \frac{s}{l}\right)q_C\right]\gamma(r) \tag{A.16}$$

where parameter s equals the length of the arc CE, l the length of the 2-node element CD, and $\gamma(r)$ is the jump function. The distance, r, in Eq. (A.16) is taken positive for particles on one side of the interface and negative for particles on the other side of the interface. For example, r for point P is negative while r for point Q is positive in Fig. A3. The jump function, $\gamma(r)$, is given by

$$\gamma(r) = \begin{cases} -\frac{1}{6}\left(\frac{|r|}{d_m}\right)^3 + \frac{1}{2}\left(\frac{|r|}{d_m}\right)^2 - \frac{1}{2}\left(\frac{|r|}{d_m}\right) + \frac{1}{6}, & \frac{|r|}{d_m} \le 1 \\ 0, & \frac{|r|}{d_m} > 1 \end{cases} \tag{A.17}$$

where d_m is a preassigned real number. Plots of the jump function and its derivative are shown in Fig. A4. One finds values of q_C and q_D as a part of the solution of the boundary-value problem. Only those particles in Ω_1 and Ω_2 whose distance from the interface AB is less than d_m contribute to the discontinuity in the normal derivative of f in Eq. (A.16). Numerical experiments suggest that a good value of d_m is four times the distance between adjacent particles in Ω_1 and Ω_2 near the interface AB.

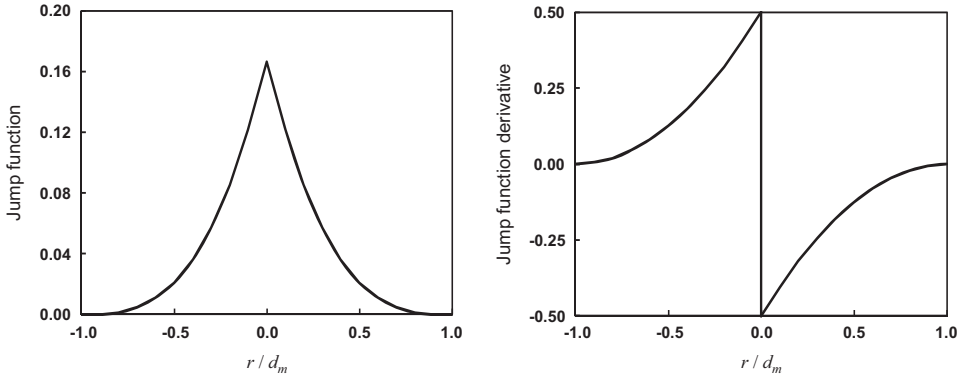

Fig. A4. Plot of the jump function and its derivative.

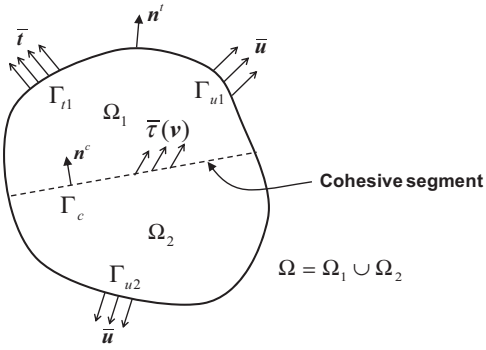

Fig. A5. Schematic sketch of the domain Ω showing a cohesive segment Γ_c, and boundaries Γ_u and Γ_t where displacement and traction boundary conditions are prescribed, respectively.

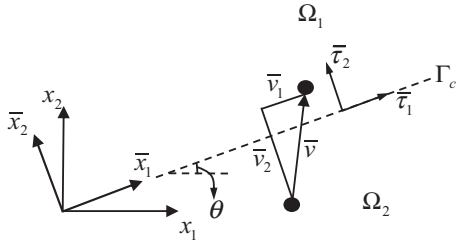

Fig. A6. Relative displacements and corresponding tractions along the cohesive segment.

A.4 Governing equations

The balance of linear momentum, in rectangular Cartesian coordinates, for static 2-D deformations of a body occupying the domain Ω is

$$\sigma_{ij,j}+b_i=0, \quad \boldsymbol{x}\in\Omega, \quad i=1,2, \tag{A.18}$$

where σ_{ij} is the Cauchy stress, b_i is the body force per unit volume, a comma followed by index i denotes partial differentiation with respect to x_i, and a repeated index implies summation over the range of the index. For simplicity, we write boundary conditions as

$$u_i=\bar{u}_i, \quad \boldsymbol{x}\in\Gamma_u, \tag{A.19}$$

$$\sigma_{ij}n_j^t=\bar{t}_i, \quad \boldsymbol{x}\in\Gamma_t, \tag{A.20}$$

$$\sigma_{ij}n_j^c=\tau_i(v_i), \quad \boldsymbol{x}\in\Gamma_c, \tag{A.21}$$

$$v_i(\boldsymbol{x})=u_{i\Omega_1}(\boldsymbol{x})-u_{i\Omega_2}(\boldsymbol{x}), \quad \boldsymbol{x}\in\Gamma_c. \tag{A.22}$$

Eqs. (A.19) and (A.20) are essential and natural boundary conditions, respectively, $\bar{u}_i$ ($\bar{t}_i$) is the prescribed displacement (traction) on the boundary $\Gamma_u(\Gamma_t)$, $n_j^t(n_j^c)$ is the unit outward normal vector to the boundary $\Gamma_t(\Gamma_c)$, and $\tau_i(v_i)$ the surface traction on the cohesive segment Γ_c where tractions depend on the displacement jump, v_i; e.g., see Fig. A5.

We introduce local rectangular Cartesian coordinate axes $\bar{x}_1$, $\bar{x}_2$ with the $\bar{x}_1$-axis aligned along Γ_c as shown in Fig. A6. For the relative displacement, v^i, in Eqs. (A.10) and (A.11) with respect to axes $\bar{x}_1$ and $\bar{x}_2$, we get

$$\bar{\boldsymbol{v}}=\begin{bmatrix}\bar{v}_1\\ \bar{v}_2\end{bmatrix}=\begin{bmatrix}\cos\theta & \sin\theta\\ -\sin\theta & \cos\theta\end{bmatrix}\begin{bmatrix}u_1^{c1}-u_1^{c2}\\ u_2^{c1}-u_2^{c2}\end{bmatrix}. \tag{A.23}$$

Here θ is the angle between x_1- and $\bar{x}_1$-coordinate axes.

Tractions from the traction–separation relation are first computed with respect to $\bar{x}_i$-coordinate axes and then transformed to the global coordinate axes.

The constitutive equation for 2-D deformations of a linear elastic homogeneous and isotropic material can be written as

$$\boldsymbol{\sigma}=\mathbf{D}\boldsymbol{\varepsilon}, \tag{A.24}$$

where $\mathbf{D}$ is the matrix of elastic constants and $\boldsymbol{\varepsilon}$ is the strain tensor corresponding to infinitesimal deformations. The 3×3 matrix $\mathbf{D}$ is given by

$$\mathbf{D}=\frac{E'}{1-\upsilon'^2}\begin{bmatrix}1 & \upsilon' & 0\\ \upsilon' & 1 & 0\\ 0 & 0 & (1-\upsilon')/2\end{bmatrix}, \tag{A.25}$$

where $E'=E/(1-\upsilon^2)$, $\upsilon'=\upsilon/(1-\upsilon)$ for plane strain, and $E'=E$, $\upsilon'=\upsilon$ for plane stress deformations; E is Young's modulus and υ is Poisson's ratio.

The strain–displacement relation is

$$\boldsymbol{\varepsilon}=\mathbf{L}\mathbf{u}, \tag{A.26}$$

where

$$\boldsymbol{\varepsilon}=\begin{bmatrix}\varepsilon_{11}\\ \varepsilon_{22}\\ 2\varepsilon_{12}\end{bmatrix}, \quad \mathbf{u}=\begin{bmatrix}u_1\\ u_2\end{bmatrix}, \quad \mathbf{L}=\begin{bmatrix}\frac{\partial}{\partial x_1} & 0\\ 0 & \frac{\partial}{\partial x_2}\\ \frac{\partial}{\partial x_2} & \frac{\partial}{\partial x_1}\end{bmatrix}, \tag{A.27}$$

and $\mathbf{u}$ is the displacement vector. Substitution for $\boldsymbol{\varepsilon}$ from Eq. (A.27) into Eq. (A.24) and the result into Eq. (A.18) gives coupled partial differential equations for u_1 and u_2 that are to be solved under boundary conditions (A.19–A.22).

Since the SSPH basis functions for spatial derivatives of a function are different from those for the function, we have

$$\mathbf{L}\mathbf{u}^I = \sum_{J=1}^{N} \left\{ \begin{bmatrix} K_{2J}^I & 0 \\ 0 & K_{3J}^I \\ K_{3J}^I & K_{2J}^I \end{bmatrix} \begin{bmatrix} \hat{u}_1^J \\ \hat{u}_2^J \end{bmatrix} \right\} \tag{A.28}$$

where $\hat{u}_1^J$ is the ficticious nodal displacement of node J in the x_1-direction.

A.5 Weak formulation of the problem

The meshless local Petrov–Galerkin (MLPG) formulation is used to find an approximate solution of the above formulated boundary-value problem. For particle I with coordinates x_i^I the weak form incorporating essential boundary conditions satisfied by the penalty method can be written as (e.g., see [15]).

$$\begin{aligned} &\int_{\Omega_1} W_{i,j}^I \sigma_{ij}\, d\Omega + \int_{\Omega_2} W_{i,j}^I \sigma_{ij}\, d\Omega + \alpha \int_{\Gamma_{u1}} W_i^I u_i\, d\Gamma + \alpha \int_{\Gamma_{u2}} W_i^I u_i\, d\Gamma - \\ &\int_{\Gamma_{u1}} W_i^I \sigma_{ij} n_j\, d\Gamma - \int_{\Gamma_{u2}} W_i^I \sigma_{ij} n_j\, d\Gamma + \int_{\Gamma_c} W_i^I \tau_i(v_i) d\Gamma = \int_{\Gamma_{t1}} W_i^I \bar{t}_i\, d\Gamma + \\ &\int_{\Gamma_{t2}} W_i^I \bar{t}_i\, d\Gamma + \alpha \int_{\Gamma_{u1}} W_i^I \bar{u}_i\, d\Gamma + \alpha \int_{\Gamma_{u2}} W_i^I \bar{u}_i\, d\Gamma + \int_{\Omega_1} W_i^I b_i\, d\Omega \\ &\quad + \int_{\Omega_2} W_i^I b_i\, d\Omega, \end{aligned} \tag{A.29}$$

where W_i^I is a test function associated with point x_i^I and α is a penalty parameter. Here Γ_c is common to Ω_1 and Ω_2, $\Gamma_{t1}, \Gamma_{u1} \in \Omega_1$ and $\Gamma_{t2}, \Gamma_{u2} \in \Omega_2$. For simplicity, α is taken to be the same for every particle on Γ_{u1} and Γ_{u2}. However, it could have been taken to be function of x_i.

For approximating the displacement field at the interface Γ_c, we place particles such that particles on Γ_c and in domain Ω_1 and Ω_2 are along the normal to Γ_c. Thus $s=0$ in Eq. (A.16), and

$$\begin{aligned} u_1(\mathbf{x}) &= \sum_{J=1}^{N} K_{1J} \hat{u}_1^J + q_1 \gamma(r), \\ u_2(\mathbf{x}) &= \sum_{J=1}^{N} K_{1J} \hat{u}_2^J + q_2 \gamma(r), \end{aligned} \tag{A.30}$$

where q_1 and q_2 are amplitudes of the jump function. Using Eqs. (A.24) and (A.26) the continuity of surface tractions on the interface give the following equation for finding q_1 and q_2.

$$q = \begin{Bmatrix} q_1 \\ q_2 \end{Bmatrix} = \sum_{J=1}^{N} \left\{ [\mathbf{A}]^{-1} [\mathbf{B}^J] \begin{bmatrix} \hat{u}_1^J \\ \hat{u}_2^J \end{bmatrix} \right\} = \sum_{J=1}^{N} \left\{ [\overline{\mathbf{q}}^J] \begin{bmatrix} \hat{u}_1^J \\ \hat{u}_2^J \end{bmatrix} \right\} \tag{A.31}$$

where

$$[\mathbf{A}] = \begin{bmatrix} A_{11} & A_{12} \\ A_{21} & A_{22} \end{bmatrix}, \quad [\boldsymbol{B}] = \begin{bmatrix} B_{11} & B_{12} \\ B_{21} & B_{22} \end{bmatrix}$$

and elements of matrices [**A**] and [**B**] are given by

$$\begin{aligned} A_{11} &= \frac{1}{2}(D_{11}^2 + D_{11}^1) n_1 \frac{\partial r}{\partial x_1} + \frac{1}{2}(D_{33}^2 + D_{33}^1) n_2 \frac{\partial r}{\partial x_2}, \\ A_{12} &= \frac{1}{2}(D_{33}^2 + D_{33}^1) n_2 \frac{\partial r}{\partial x_1} + \frac{1}{2}(D_{12}^2 + D_{12}^1) n_1 \frac{\partial r}{\partial x_2}, \\ A_{21} &= \frac{1}{2}(D_{33}^2 + D_{33}^1) n_1 \frac{\partial r}{\partial x_2} + \frac{1}{2}(D_{21}^2 + D_{21}^1) n_2 \frac{\partial r}{\partial x_1}, \\ A_{22} &= \frac{1}{2}(D_{33}^2 + D_{33}^1) n_1 \frac{\partial r}{\partial x_1} + \frac{1}{2}(D_{22}^2 + D_{22}^1) n_2 \frac{\partial r}{\partial x_2}, \\ B_{11}^J &= (D_{11}^1 - D_{11}^2) n_1 K_{2J} + (D_{33}^1 - D_{33}^2) n_2 K_{3J}, \\ B_{12}^J &= (D_{12}^1 - D_{12}^2) n_1 K_{3J} + (D_{33}^1 - D_{33}^2) n_2 K_{2J}, \\ B_{21}^J &= (D_{33}^1 - D_{33}^2) n_1 K_{3J} + (D_{21}^1 - D_{21}^2) n_2 K_{2J}, \\ B_{22}^J &= (D_{33}^1 - D_{33}^2) n_1 K_{2J} + (D_{22}^1 - D_{22}^2) n_2 K_{3J}, \end{aligned}$$

where $\boldsymbol{n}^s = \begin{Bmatrix} n_1 \\ n_2 \end{Bmatrix}$ is the normal vector on the interface,

$$[\mathbf{D}^1] = \begin{bmatrix} D_{11}^1 & D_{12}^1 & 0 \\ D_{21}^1 & D_{22}^1 & 0 \\ 0 & 0 & D_{33}^1 \end{bmatrix}, \quad [\mathbf{D}^2] = \begin{bmatrix} D_{11}^2 & D_{12}^2 & 0 \\ D_{21}^2 & D_{22}^2 & 0 \\ 0 & 0 & D_{33}^2 \end{bmatrix},$$

are elastic constants for materials of sub-domains, Ω_1 and Ω_2, respectively.

Overlapping particles from domains Ω_1 and $\Omega_2$are placed on the cohesive segment region. Substitution from Eqs. (A.24), (A.26) and (A.30) into Eq. (A.29) gives

$$\sum_{J=1}^{N} (\boldsymbol{K}_{IJ}' + \boldsymbol{K}_{IJ}'') \hat{\boldsymbol{u}}^J = \boldsymbol{F}_I \tag{A.32}$$

where

$$\begin{aligned} \boldsymbol{K}_{IJ}' &= \int_{\Omega_1} (\boldsymbol{L}\boldsymbol{W}^I)^T \boldsymbol{D} \boldsymbol{V}_J\, d\Omega + \int_{\Omega_2} (\boldsymbol{L}\boldsymbol{W}^I)^T \boldsymbol{D} \boldsymbol{V}_J\, d\Omega + \alpha \int_{\Gamma_{u1}} \boldsymbol{W}^I \boldsymbol{M}_J\, d\Gamma \\ &\quad + \alpha \int_{\Gamma_{u2}} \boldsymbol{W}^I \boldsymbol{M}_J\, d\Gamma - \int_{\Gamma_{u1}} \boldsymbol{W}^I \boldsymbol{N} \boldsymbol{D} \boldsymbol{V}_J\, d\Gamma - \int_{\Gamma_{u2}} \boldsymbol{W}^I \boldsymbol{N} \boldsymbol{D} \boldsymbol{V}_J\, d\Gamma, \\ \boldsymbol{K}_{IJ}'' &= \begin{cases} \int_{\Gamma_c} \boldsymbol{W}^I \boldsymbol{S} \boldsymbol{\Phi}_J\, d\Gamma, & \overline{\boldsymbol{v}} < \boldsymbol{v}_0, \\ -\int_{\Gamma_c} \boldsymbol{W}^I \boldsymbol{T}' \boldsymbol{\Phi}_J\, d\Gamma, & \overline{\boldsymbol{v}} > \boldsymbol{v}_0, \end{cases} \\ \boldsymbol{F}_I &= \begin{cases} \overline{\boldsymbol{F}}_I, & \overline{\boldsymbol{v}} < \boldsymbol{v}_0, \\ \overline{\boldsymbol{F}}_I - \int_{\Gamma_c} \boldsymbol{W}^I \overline{\boldsymbol{T}}\, d\Gamma & \overline{\boldsymbol{v}} > \boldsymbol{v}_0, \end{cases} \\ \overline{\boldsymbol{F}}_I &= \int_{\Gamma_{t1}} \boldsymbol{W}^I \overline{\boldsymbol{t}}\, d\Gamma + \int_{\Gamma_{t2}} \boldsymbol{W}^I \overline{\boldsymbol{t}}\, d\Gamma + \int_{\Omega_1} \boldsymbol{W}^I \boldsymbol{b}\, d\Omega + \int_{\Omega_2} \boldsymbol{W}^I \boldsymbol{b}\, d\Omega \\ &\quad + \alpha \int_{\Gamma_{u1}} \boldsymbol{W}^I \overline{\boldsymbol{u}}\, d\Gamma + \alpha \int_{\Gamma_{u2}} \boldsymbol{W}^I \overline{\boldsymbol{u}}\, d\Gamma, \\ \boldsymbol{W}^I &= \begin{bmatrix} W^I & 0 \\ 0 & W^I \end{bmatrix}, \boldsymbol{V}_J = \begin{bmatrix} K_{2J}^I + \overline{q}_{1J}^I \frac{\partial \gamma(r^I)}{\partial x_1} & 0 \\ 0 & K_{3J}^I + \overline{q}_{2J}^I \frac{\partial \gamma(r^I)}{\partial x_2} \\ K_{3J}^I + \overline{q}_{2J}^I \frac{\partial \gamma(r^I)}{\partial x_2} & K_{2J}^I + \overline{q}_{1J}^I \frac{\partial \gamma(r^I)}{\partial x_1} \end{bmatrix}, \boldsymbol{S} = \begin{bmatrix} S_0^{II} & 0 \\ 0 & S_0^I \end{bmatrix}, \end{aligned}$$

$$\boldsymbol{T}' = \begin{bmatrix} \frac{\tau_{cr}^{II}}{(v_f^{II} - v_0^{II})} & 0 \\ 0 & \frac{\tau_{cr}^{I}}{(v_f^{I} - v_0^{I})} \end{bmatrix}, \overline{\boldsymbol{T}} = \begin{Bmatrix} \frac{v_f^{II} \tau_{cr}^{II}}{(v_f^{II} - v_0^{II})} \\ \frac{v_f^{I} \tau_{cr}^{I}}{(v_f^{I} - v_0^{I})} \end{Bmatrix}, \boldsymbol{v}_0 = \begin{Bmatrix} v_0^{II} \\ v_0^{I} \end{Bmatrix},$$

$$\boldsymbol{M}_J = \begin{bmatrix} K_{1J}^I + \overline{q}_{1J}^I \gamma(r^I) & 0 \\ 0 & K_{1J}^I + \overline{q}_{2J}^I \gamma(r^I) \end{bmatrix}, \boldsymbol{N} = \begin{bmatrix} n_1 & 0 & n_2 \\ 0 & n_2 & n_1 \end{bmatrix},$$

$$\boldsymbol{\Phi}_J = \begin{bmatrix} K_{1J}^{c1} & 0 & -K_{1J}^{c2} & 0 \\ 0 & K_{1J}^{c1} & 0 & -K_{1J}^{c2} \end{bmatrix}.$$

K_{1J}^{c1} and K_{1J}^{c2} are the SSPH basis functions for particles located on the boundaries Γ_{c1} and Γ_{c2}, respectively. We derive an algebraic equation similar to Eq. (A.32) for each particle in the domain Ω, thereby obtain the following system of equations.

$$[\mathbf{K}]\{\mathbf{U}\} = \{\mathbf{F}\}, \tag{A.33}$$

where N_{Ω_1} and N_{Ω_2} are number of particles for domains Ω_1 and Ω_2, respectively.

$$\mathbf{U} = \begin{bmatrix} \mathbf{U}_{\Omega_1} \\ \mathbf{U}_{\Omega_2} \end{bmatrix}, \mathbf{U}_{\Omega_1} = \begin{bmatrix} u_1^1 \\ u_2^1 \\ \vdots \\ u_1^{N_{\Omega_1}} \\ u_2^{N_{\Omega_1}} \end{bmatrix}, \mathbf{U}_{\Omega_2} = \begin{bmatrix} u_1^1 \\ u_2^1 \\ \vdots \\ u_1^{N_{\Omega_2}} \\ u_2^{N_{\Omega_2}} \end{bmatrix}$$

N_{Ω_1} and N_{Ω_2} are number of particles for domains Ω_1 and Ω_2, respectively.

References

[1] Barenblatt GI. The mathematical theory of equilibrium cracks in brittle fracture. Adv Appl Mech 1962:55–129.
[2] Dugdale DS. Yielding of steel sheets containing slits. J Mech Phys Solids 1960;8:100–4.
[3] Xu XP, Needleman A. Numerical simulations of fast crack-growth in brittle solids. J Mech Phys Solids 1994;42(9):1397–434.
[4] Remmers JJC, de Borst R, Needleman A. A cohesive segments method for the simulation of crack growth. Comput Mech 2003;31(1–2):69–77.
[5] Elices M, et al. The cohesive zone model: advantages, limitations and challenges. Eng Fract Mech 2002;69(2):137–63.
[6] Hattiangadi A, Siegmund T. A thermomechanical cohesive zone model for bridged delamination cracks. J Mech Phys Solids 2004;52(3):533–66.
[7] Klein PA, et al. Physics-based modeling of brittle fracture: cohesive formulations and the application of meshfree methods. Theor Appl Fract Mech 2001;37(1–3):99–166.
[8] Li H, Chandra N. Analysis of crack growth and crack-tip plasticity in ductile materials using cohesive zone models. Int J Plast 2003;19(6):849–82.
[9] Sorensen BF, Jacobsen TK. Characterizing delamination of fibre composites by mixed mode cohesive laws. Compos Sci Technol 2009;69(3–4):445–56.
[10] Zhang ZYJ, Paulino GH. Cohesive zone modeling of dynamic failure in homogeneous and functionally graded materials. Int J Plast 2005;21 (6):1195–254.
[11] Love BM, Batra RC. Effect of particulate/matrix debonding on the formation of adiabatic shear bands. Int J Mech Sci 2010;52(2):386–97.
[12] Sun YZ, Hu YG, Liew KM. A mesh-free simulation of cracking and failure using the cohesive segments method. Int J Eng Sci 2007;45(2–8):541–53.
[13] Barbieri E, Meo M. A meshless cohesive segments method for crack initiation and propagation in composites. Appl Compos Mater 2011;18(1):45–63.
[14] Batra RC, Zhang GM. SSPH basis functions for meshless methods, and comparison of solutions with strong and weak formulations. Comput Mech 2008;41(4):527–45.
[15] Tsai CL, Guan YL, Batra RC, Ohanehi DC, Dillard JG, Nicoli E, Dillard DA. Comparison of the performance of SSPH and MLS basis functions for two-dimensional linear elastostatics problems including quasistatic crack propagation. Comput Mech 2013;51:19–34.
[16] De Moura MFSF, et al. Cohesive and continuum mixed-mode damage models applied to the simulation of the mechanical behaviour of bonded joints. Int J Adhes Adhes 2008;28(8):419–26.
[17] Krongauz Y, Belytschko T. EFG approximation with discontinuous derivatives. Int J NumerMethods Eng 1998;41(7):1215–33.
[18] Batra RC, Porfiri M, Spinello D. Treatment of material discontinuity in two meshless local Petrov–Galerkin (MLPG) formulations of axisymmetric transient heat conduction. Int J Numer Methods Eng 2004;61(14):2461–79.
[19] Dillard, DA, et al. A dual-actuator load frame for mixed-mode fracture of laminated or adhesively bonded specimens. In: Proceedings of the society for experimental mechanics. St. Louis: Society for Experimental Mechanics; 2006.
[20] Singh HK, et al. Mixed mode fracture testing of adhesively bonded wood specimens using a dual actuator load frame. Holzforschung 2010;64 (3):353–61.
[21] Blackman BRK, et al. Measuring the mode I adhesive fracture energy, G(IC), of structural adhesive joints: the results of an international round-robin. Int J Adhes Adhes 2003;23(4):293–305.
[22] Blackman BRK, Kinloch AJ, Paraschl M. The determination of the mode II adhesive fracture resistance, G(IIC), of structural adhesive joints: an effective crack length approach. Eng Fract Mech 2005;72(6):877–97.
[23] Batra RC, Liang XQ. Finite dynamic deformations of smart structures. Comput Mech 1997;20(5):427–38.
[24] Batra RC, Love BM. Multiscale analysis of adiabatic shear bands in tungsten heavy alloy particulate composites. Int J Multiscale Comput Eng 2006;4 (1):95–114.
[25] Pirondi, A. and G. Nicoletto. Comportamento a frattura di un adesivo strutturale. In: Proceedings of the 15th national congress of the italian group of fracture; 2000.
[26] Alfano M, et al. Mode I fracture of adhesive joints using tailored cohesive zone models. Int J Fract 2009;157(1–2):193–204.
[27] Sack J, Welch WJ, Mitchell TJ. Design and analysis of computer experiments. J R Soc StatSci 1989;4:409–35.
[28] Davies P, et al. Comparison of test configurations for determination of mode II interlaminar fracture toughness results from international collaborative test programme. Plast Rubber Compos 1999;28(9):432–7.
[29] Lee SM. Mode II delamination failure mechanisms of polymer matrix composites. J Mater Sci 1997;32(5):1287–95.
[30] Ameli A, et al. Crack path selection in the fracture of fresh and degraded epoxy adhesive joints. Eng Fract Mech 2011;78(9):1986–2003.
[31] Qian LF, Batra RC. Transient thermoelastic deformations of a thick functionally graded plate. J. Therm Stresses 2004;27:705–40.
[32] Blackman BRK, et al. The use of a cohesive zone model to study the fracture of fibre composites and adhesively-bonded joints. Int J Fract 2003;119:25–46.
[33] Álvarez, D et al., Mode II fracture in adhesive joints. In: Proceedings of the 2013 adhesion society meeting, Daytona, FL; 2013.
[34] Batra RC, Porfiri M, Spinello D. Free and forced vibrations of a segmented bar by a meshless local Petrov–Galerkin (MLPG) formulation. Comput Mech 2008;41:473–91.